Helium-Ion Induced Deposition: Modelling Nanopillar Growth with a Moving Ion Beam

Johannes van den Berg

May 2021

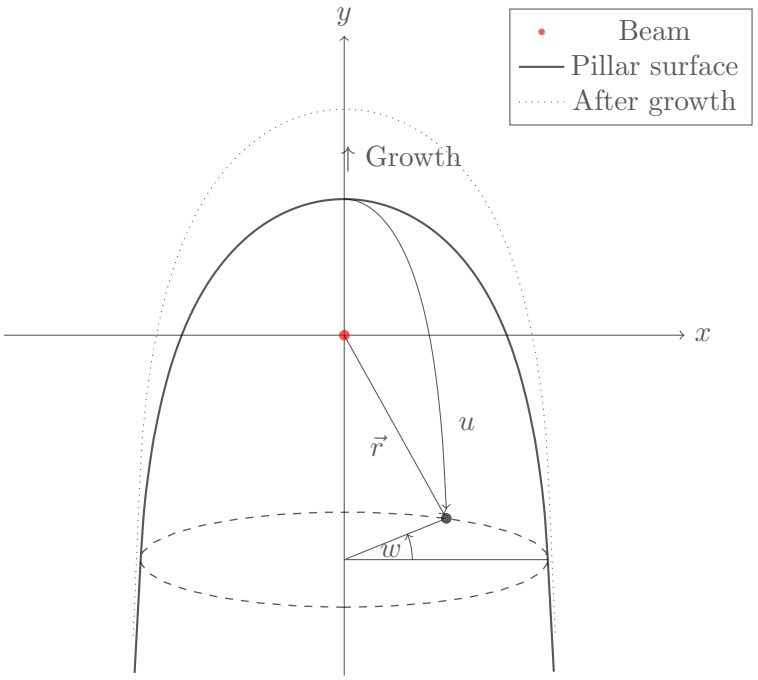

in efforts of the attainment of the degrees
Bachelor of Science in Applied Physics and
Bachelor of Science in Applied Mathematics
from the Delft University of Technology.

Under the supervision of
Dr. P.F.A. Alkemade
Dr. J.L.A. Dubbeldam

TU Delft

Abstract

Helium-ion induced deposition (He-IBID) is a small-scale manufacturing technique that uses a helium microscope to focus a helium-ion beam onto an adsorbed precursor gas, causing nanometer-scaled depositions onto a substrate. However, due to local depletion of the precursor gas, the amount of deposition can not be expected to be proportional to the beam current. The mechanisms of this growth need to be well investigated to understand the limitations and capabilities of this technique.

Most studies look at simple pillar growth with a stationary beam, and most models exclude the surface diffusion of precursor molecules. We attempt to model the growth of horizontally grown pillars using a horizontally moving ion beam. According to experiments with this type of growth [1], precursor surface diffusion is a key mechanism, and thus past studies may not be sufficient.

We use develop a continuum model based on solving differential equations. One benefit over the more common Monte Carlo methods is that the effect of the various mechanisms are more explicitly written in differential equation form. Another benefit is that the simulation is differentiable, lending itself to better application of new differentiable programming techniques. One difficulty, however, is in the accurate modelling of the energy-dependent interactions with a source that has varying electron energies.

We derive a system of ordinary differential equations to model a simplified two-dimensional approach and an approximation for an effective secondary electron flux to use in decomposition rate calculations. We investigate the available literature to find realistic values for the physical and operational parameters required to calculate solutions. Through numerical integration we find solutions and show how the model estimates pillar width changes when these parameters are altered.

We use numerical integration to solve the ODE system, and present the results. We find a nucleation boundary—dependent on the beam movement speed and current—below which pillars cannot be grown, consistent with experiment [1].

We find that the assumptions made in the surface diffusion calculation are too extreme, and that likely solving a PDE system of the full surface in three-dimensional space will be required for accurate results.

Contents

1 Introduction

Although the development of mechanical computers and vacuum tube computers might have empowered the owners of such magical devices, and vacuum tubes greatly assisted the proliferation of long distance communication such as radio and telephone, they were too expensive and lacked the raw computational power to truly change the world. The development of the semiconductor transistor—along with many other technologies—greatly decreased the attainable size and cost of commercially available processors and computer memory, and it is this that made the information age possible.

That the oft paraphrased Moore's law (that the number of transistors in a dense integrated circuit doubles every one to two years) has been followed for over 50 years stands testament to the importance assigned to the minification of these semiconductor devices even now. Indeed, many techniques have been developed for the fabrication of circuitry and tools on the micro- and nanoscale, the most important of which are photolithography, soft lithography, film deposition, etching, and bonding [2].

This study focuses on the nanofabrication technique Ion-Beam-Induced Deposition (IBID), a.k.a. Focused Ion Beam Chemical Vapour Deposition (FIB-CVD), which is a variant of the more pervasive method Electron-Beam-Induced Deposition (EBID). IBID is the process of using a ion beam to locally decompose gaseous precursor molecules adhered to a substrate to cause local deposition of products of the decomposition onto said substrate; the beam can be moved relative to the substrate to create three dimensional structures. [graphic here] In particular, the assumptions made in this study are such that the results pertain especially to He-IBID, where helium ions are used as a beam source. A focused beam of helium ions—as opposed to electrons and gallium ions—provides better spatial resolution and is back-scattered and deflected less, making it easier to control where deposition occurs.

In terms of practical applications, IBID is used in integrated circuit modification through "deposition of either metallic or insulating materials to either modify existing or to create new structures" and also in "producing small quantity prototypes which would require substantial investments in other methods" [3]. Similar to the production of prototypes, IBID is also used in the creation of experimental setups for research into the electrical and mechanical behaviour of nanoscale structures. [references here] [hammerhead afm probe] [photonic crystal]

Directing a stationary helium ion beam directly onto a substrate that is continuously fed a precursor gas results in the growth of a pillar of 30 to 60 nm width with common beam current values. This is much smaller than achievable with the more common electron- and gallium ion beam induced deposition because of the negligible scattering of primary particles and the negligible sputtering in the case of helium [4]. Since the substrate is growing along the direction of the beam, the helium ions continue to travel on the inside of the pillar, causing sideways growth.

Even smaller "nanoneedles" are achievable by moving ion beam pillar growth. The beam is oriented so that it just grazes a feature on the substrate, and then moved away from the substrate at a controlled speed (see Figure 2). The beam passes through the tip of the growing needle such that scattering is minimal and deposition is localised to the extreme end of the tip. By optimising the speed of the beam movement, a needle width of 13nm has been achieved [1].

Utilising the horizontal growth mode of IBID, many complex structures can be fabricated. [pictures] [5]

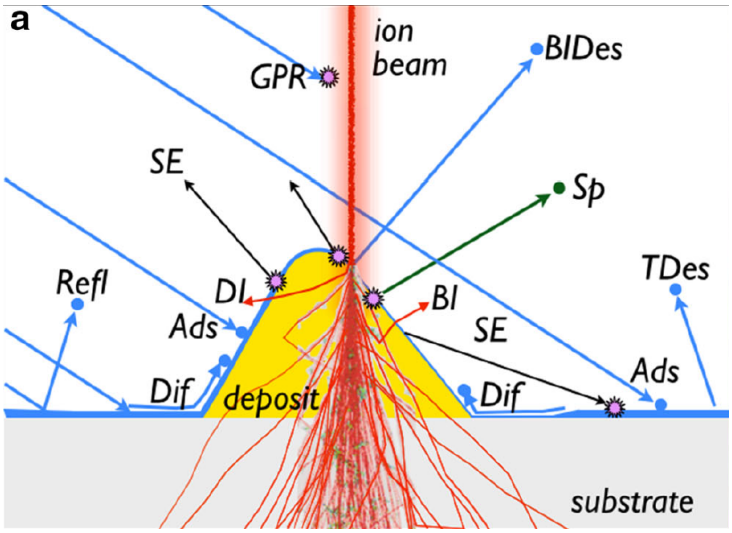

Figure 1: Ion beam induced deposition and related mechanisms. Used with permission from [4].

Refl	Impinging precursors may reflect off instead of adsorbing, especially if the surface is saturated.
Dif	The precursors diffuse over the surface towards the depleted areas.
Ads	Impinging precursors has a chance to adsorb onto the surface if it is not saturated.
DI	Deflected ion.
SE	Secondary electrons that reach the surface are the primary mechanism for decomposition.
GPR	Gas-phase reaction. Rare event.
BIDes	Beam induced desorption.
Sp	Sputtering. High energy ions may cause ejection of atoms from the deposit.
BI	Backscattered ion.
TDes	Thermal desorption—also referred to as spontaneous desorption. Standard evaporation that would occur regardless of the ion beam.

1.1 The IBID process

IBID starts with a substrate kept under vacuum. A precursor gas for (metal) deposition such as Trimethyl(methylcyclopentadienyl)platinum (MeCpPtMe3) is then fed onto the substrate via a gas injection system ending in a thin pipe that can be brought to within 100 µm from the substrate surface. The gas molecules have a tendency to adhere to the surface in a monolayer; the surface can be saturated (Langmuir adsorption).

When an energetic particle collides with a precursor gas molecule, the gas molecule breaks up into volatile and non-volatile components. This is called decomposition. The volatile molecules drift off into the vacuum. If this occurs while the molecule is adhered to a surface, the non-volatile components bond with that surface.[1] This is called deposition.

To cause this deposition, an ion beam is focused onto the substrate covered in precursor gas molecules. However, the direct interaction between the ions and the gas molecules has a negligible cross-section; the ions mostly pass through the adsorbed precursor layer and generate secondary electrons as they travel through the substrate. If these generated electrons reach the surface, they can interact with the precursor molecules to cause the deposition. Typical He ions (30 keV) travel 100 nm in solids, while their SEs travel around 1 nm in metals or 10-20 nm in insulators.

The secondary electrons can also stimulate the precursor molecules to desorb from the surface when they do not decompose. As opposed to this stimulated desorption, there is also spontaneous/thermal desorption, which has the same probability of occurring for each adsorbed molecule, regardless of electron flux.

While adhered, precursor molecules freely move across the surface, colliding with other precursor molecules. Diffusion plays an important role in restoring depleted areas of precursor molecules.

Indeed, a complete model the IBID process will need to keep track of all these mechanisms:

- Secondary electron production
- Precursor
  - adsorption (due to the gas feed)
  - decomposition
  - desorption (spontaneous & stimulated)
  - diffusion over the surface
- Surface growth due to deposition

This study will set up a model of the steady state horizontal growth mode through differential equations. It will then attempt—through the solving of differential equations—to find the pillar width given a set of realistic parameters (including beam power, beam/growth speed, precursor diffusion constant, etc.), and observing the change incurred when the parameters are altered.

[1] In the case of MeCpPtMe3, 8-20% of the deposition consists of platinum. [4]

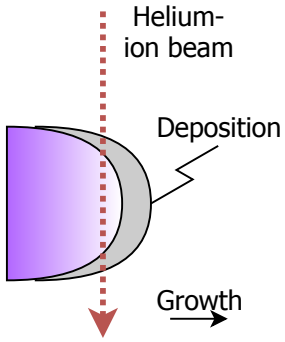

Figure 2: He-IBID moving ion beam pillar growth

2 Theory

2.1 Previous Models and Simulations

In this section we will describe existing models and simulations of IBID (and some relevant ones of EBID).

2.1.1 Utke

In the 2008 review article [6], Utke et al. exhibit continuum models which investigate deposition in the case of a focused ion (or electron) beam incident on a flat substrate. Dimensionless variables are introduced and used to classify process regimes based on the limiting factor in precursor dissociation. Unfortunately, the models assume flat geometry and that dissociation occurs proportionally to the ion flux (with no mention of secondary electrons), making the results not directly applicable to our situation.

Monte Carlo models for EBID are also presented, but at the time of the review article, no MC simulations were reported for IBID.

2.1.2 Monte Carlo (Philip Rack)

A series of Monte Carlo simulations of HeIBID pillar growth was completed by Smith et al. in 2010 [7] with a custom-built program called EnvisION. The simulation tracks the path and interactions of Helium ions into the substrate, where secondary electrons are generated and subsequently tracked.

This model only deals with pillars grown via a stationary beam. It also assumes no surface diffusion of precursors; only (non-directional) adsorption from the gas phase contributes to precursor repletion. However, with moving ion beam pillars, diffusion plays an important role in precursor repletion [1].

A more detailed description of the implementation of the MC simulation can be found in [8].

In 2013 another Monte Carlo simulation was carried out to compare depositions caused by Helium and Neon ions [9]. The results indicated that a Neon ion beam has a smaller interaction region (and thus deposits thinner pillars).

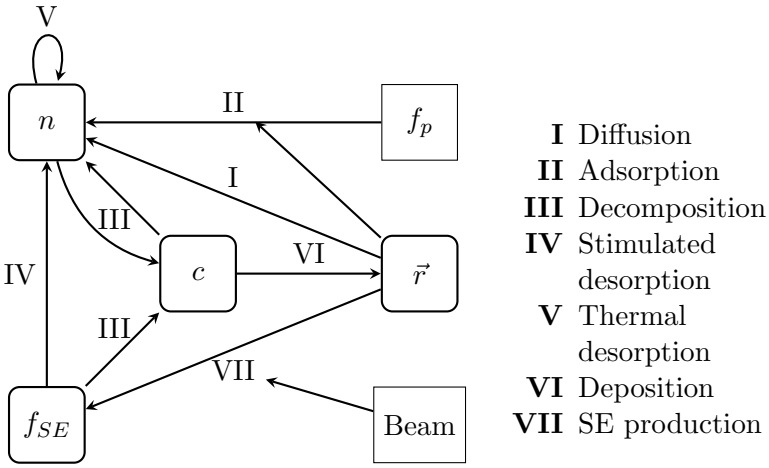

Figure 3: Overview of the variables and the mechanisms in He-IBID
n [-] is the precursor coverage; it measures how covered the surface is in precursors from 0 to 1 (empty to full monolayer).
f_p [prec./nm^2] is the flux of the precursors from the gas-injection system onto the surface.
c [/ms] is the precursor decomposition rate in monolayers per unit time.
$\vec{r}$ [nm] indicates the location/shape of the surface.
f_{SE} [elec./nm^2] is the secondary electron flux on the surface due to the ion beam.

Similar to the earlier Monte Carlo experiments, stationary beams and a lack of surface diffusion were assumed. Due to these two points, the results of these simulations are not directly applicable, but if surface diffusion was to be added, the EnvisION program may provide some powerful insight to growth using moving ion beams.

2.1.3 Alkemade model

A 2010 paper [10] an analytical model for pillars grown perpendicular to the substrate was derived and fit to experiment. It was used to describe vertical, lateral and volumetric growth rates as functions of beam current, and for calculating ion deposition efficiency, which was found to be only weakly dependent on beam current. However, [1] does see some change in efficiency when changing the speed of the beam in the growth of horizontal pillars. This indicates that the growth mechanism is qualitatively different. This paper also identified the distinct precursor-limited and ion-limited growth regimes.

An overview from 2014 [4] presented various insights. It wrote mechanisms contributing to precursor coverage rate of change as terms in a differential equation, which will be presented in the following section. It also included an important estimation of the effective cross-section and the diffusion constant using empirical data.

2.2 Equations governing He-IBID

The diagram in figure 3 shows the mechanisms that relate and affect these state variables. Note that only the precursor coverage n has more than one mechanism affecting it. To facilitate the description of each mechanism separately, we write the rate of change in precursor coverage as a sum, where each term denotes the contribution of a separate mechanism:

$$\frac{\partial n}{\partial t} = \sum_i m_i \tag{1}$$

Each mechanism is ascribed an equation that describes its behaviour. The time-dependency of the state/input variables in each of these equations is implicit.

2.2.1 I - Diffusion

$$m_{\mathrm{I}} = D\nabla_S^2 n \tag{2}$$

Where n is the precursor coverage, D is the diffusion constant, ∇_S^2 is the Laplace-Beltrami operator for surfaces.

The dependency on the surface $\vec{r}$ is not directly visible in the equation; it is hidden in the ∇_S^2 symbol, as the surface derivative is directly dependent on the metric of the surface; for any scalar field $\phi(\vec{u})$ [11],

$$\nabla_S^2 \phi = \frac{1}{\sqrt{g}} \frac{\partial}{\partial u^i} \left(\sqrt{g} g^{ij} \frac{\partial \phi}{\partial u^j} \right). \tag{3}$$

Where g is the metric, u^i indicates the ith component of $\vec{u}$ and the Einstein summation convention is used.

2.2.2 II - Adsorption

Assuming the precursors impinge at a constant angle and flux across the entire work area,

$$m_{\mathrm{II}} = \mathbb{1}_p(\vec{r}) \frac{s}{n_{sat}} (1 - n) \vec{f_p} \cdot \vec{N}. \tag{4}$$

$$\mathbb{1}_p(\vec{r}) = \begin{cases} 1 & \text{if } \vec{r} \text{ visible by } \vec{f_p} \\ 0 & \text{otherwise} \end{cases}$$

Where s is the probability of an impinging precursor sticking to an unoccupied site, $\vec{f_p}$ is the flux of impinging precursors, n_{sat} is the maximal precursor density, and $\vec{N}$ is the outward pointing surface normal.

We say $\mathbb{1}_p(\vec{r}) = 1$ when the impinging precursors can reach that part of the surface $\vec{r}$, i.e. there is not another part of the surface blocking off the precursor supply.[2]

2.2.3 III - Decomposition

Arguably the most important mechanism; it is the only one where two state variables are used to define another, and the only which affects multiple state variables.

$$c = \sigma^{eff} n f_{SE} \tag{5}$$

$$m_{\mathrm{III}} = -c$$

A straightforward product of n and f_{SE} with the effective cross-section σ^{eff} gives the decomposition rate (of precursor monolayers) c, which in turn causes a diminishment of precursor coverage.

[2] A more rigorous definition that may be useful for computation is the following. We define a point on the surface $\vec{p} \in \vec{r}[U]$ to be visible by a vector $\vec{f} \in \mathbb{R}^3$ when $\max\{\, k \mid -k\vec{f} + \vec{p} \in \vec{r}[U] \,\} = 0$

2.2.4 IV - Stimulated desorption

$$m_{\mathrm{IV}} = -\sigma^{des} n f_{SE} \tag{6}$$

Where σ^{des} is the cross-section of SEs causing precursors to unstick from the surface without decomposing.

2.2.5 V - Thermal desorption

Thermal excitations occasionally exceed the adhesion energy of the precursor molecules, causing the molecules to escape into to the vacuum chamber. The rate at which this happens depends on the surface temperature, which may vary over time.

$$m_{\mathrm{V}} = -\frac{n}{\tau_{des}} \tag{7}$$

τ_{des} is the average time for thermal desorption of a precursor molecule which can be calculated from the temperature and desorption energy.

2.2.6 VI - Deposition

The volumetric deposition rate (per area) is the product of the volume per decomposition V_p and the decomposition rate (per area) c:

$$\frac{d(V/\delta A)}{dt} = V_p n_{sat} c \tag{8}$$

We must use results from differential geometry to then relate the local volumetric deposition to a change in the local surface to find how the surface is actually evolving given some amount of deposition. As discussed in Deserno [11], this can be calculated for example via the mean curvature of the surface. Later we will be making assumptions such that the variation in the surface is constant over the surface, leading to a much simpler relation.

2.2.7 VII - SE production

Assuming an infinitesimally thin ion beam which has isotropic production of secondary electrons along its trajectory in the solid, and that the momentum of an SE remains unchanged after emission (besides completely stopping), the SE flux can be calculated on the surface as

$$f_{SE}(\vec{r}) = \frac{I}{q_e} N_{SE} \int_{\mathcal{B}} e^{-\frac{|\vec{r'}|}{\lambda_e}} \frac{1}{|\vec{r'}|^2} \, d\vec{b} \tag{9}$$

$$\text{with } \vec{r'} = \vec{r} - \vec{b}$$

Where I is the beam current, q_e is the elementary charge, N_{SE} is the number of secondary electrons generated per unit distance per ion, $\vec{b} \in \mathcal{B}$ indicate points on the He ion beam path inside the pillar, and λ_e is the inelastic mean free path of the SEs.

The integrand consists of three factors each with their own reasoning behind them:

$\frac{I}{q_e} N_{SE}$ Rate of secondary electron generation per unit distance along the beam [$\mathrm{SEs\,m^{-1}\,s^{-1}}$]

$e^{-\frac{|\vec{r'}|}{\lambda_e}}$ Limited penetration distance of SEs (exponential decay)

$|\vec{r'}|^{-2}$ Inverse square law (spreading out from a point source)

3 The stable form of the simplified 2D problem

As the pillar is grown further from the substrate, its fixed width implies that the growth (and thus decomposition) reaches some equilibrium. We want investigate this stable state of the horizontal growth mode–and whether it exists under the assumptions of our model. In search of the stable growth state, we look for solutions that satisfy $\frac{\partial n}{\partial t} = 0$, and we restrict the growth of the surface to to one that retains the shape of the surface over time (just shifted in the direction of growth).

To define our surface, we will use a geodesic polar parameterisation with the tip of the pillar ($u = 0$) being the origin, and $w = 0$ corresponding to the cross-section perpendicular to the ion beam (for $x > 0$).

$$\vec{r}(u, w) = \begin{bmatrix} x(u, w) \\ y(u, w) \\ z(u, w) \end{bmatrix} \tag{10}$$

with the metric

$$g = \begin{bmatrix} 1 & 0 \\ 0 & x_w^2 + y_w^2 + z_w^2 \end{bmatrix} \tag{11}$$

where $g_{11} = 1$ is called the arc-length restriction ($|\vec{r}_u| = 1$) and $g_{12} = g_{21} = 0$ is called the orthogonality restriction.

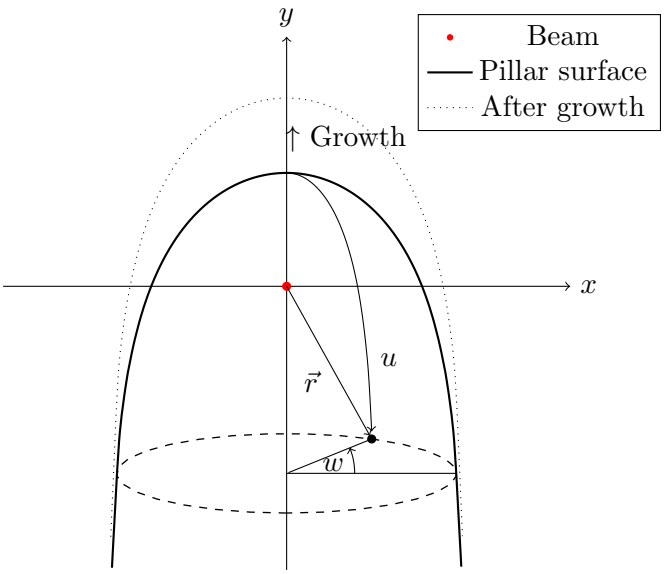

Figure 4: Diagram of the geodesic polar parametrisation of the pillar surface at the tip. The beam at the graph origin points into the page. y indicates the direction of growth. For a given w, u is the arc-length of a geodesic that extends from the tip of the pillar at an angle of w.

To simplify matters, we look at the surface cross-section perpendicular to the beam with only the suspected key mechanisms included:

I Diffusion

II Adsorption

III Decomposition

VI Deposition

VII SE production

That is to say, we leave out both spontaneous/thermal and stimulated desorption effects. While we are only looking at a cross-section, there is still significant diffusion perpendicular to this plane (later referred to as angular diffusion, as per the angular coordinate w). The diffusion (and some minor relevance to the volumetric surface growth) is why a three-coordinate system will still be required for some steps in the derivation.

3.1 Adapting Equations for the Model

Now we take the equations governing each mechanism, adapt and make simplifying assumptions according to the situation of stable growth in 2D.

3.1.1 I - Diffusion

For the diffusion term we have (from equation 3)

$$m_{\mathrm{I}} = D\nabla_S^2 n = \frac{D}{\sqrt{g}} \frac{\partial}{\partial u^i} \left(\sqrt{g} g^{ij} \frac{\partial n}{\partial u^j} \right).$$

The inverse metric values for our parametrisation are $g^{11} = 1$ and $g^{22} = \frac{1}{x_w^2 + y_w^2 + z_w^2}$, and the root of the determinant of the metric is $\sqrt{g} = \sqrt{g_{22}}$. Since the non-diagonal values of the metric are zero, we get

$$m_{\mathrm{I}} = D\nabla_S^2 n = \frac{D}{\sqrt{g}} \left((\sqrt{g} n_u)_u + (\sqrt{g} g^{22} n_w)_w \right). \tag{12}$$

This can be expanded and simplified further by accounting for symmetry when on the cross-section $w = 0$. Since the cross-section is perpendicular to the beam, the shape and precursor distribution of the pillar in this model must follow mirror symmetry across the plane of the cross-section $z = 0$. And so, odd-ordered w-derivatives of x, y, n and their u-derivatives are zero, and even-ordered w-derivatives of z and its u-derivatives are zero.

3.1.2 II - Adsorption

For the impinging precursor adsorption term we have

$$m_{\mathrm{II}} = \mathbb{1}_p(\vec{r}) \frac{s}{n_{sat}} (1 - n) \left| \vec{f_p} \cdot \vec{N} \right|.$$

To remove the positional dependency–leaving only dependency on n–we assume the following:

- $\vec{f_p}(\vec{r})$ has a constant magnitude f_p over the area where the pillar is growing, also taking into account the angle of incidence. (In reality the magnitude varies significantly based on the position relative to the needle of the gas injection system, but not on the scale of pillar-lengths.)
- The pillar is approximately cylindrical, so that the ratio of side-profile area (visible to impinging precursor molecules) to surface area is everywhere $1 : \pi$.
- The pillar is long and thin, so diffusion around the circumference of the pillar occurs relatively instantaneously. (And thus adsorption causes increase in coverage around the whole circumference at the same time.)

From these assumptions, we can derive the adsorption source term to be

$$m_{\mathrm{II}} = \frac{s f_p}{\pi n_{sat}} (1 - n) = \frac{\gamma}{n_{sat}} (1 - n). \tag{13}$$

where γ is the rate of precursor density per fraction of empty precursor sites on the pillar surface due to adsorption.

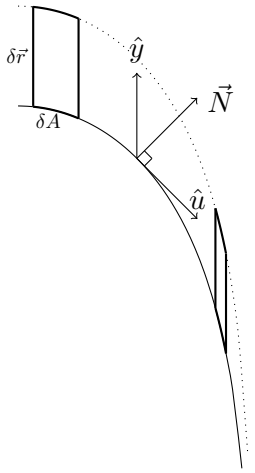

Figure 5: Everywhere equal growth in the y direction: The normal $\vec{N}$ flattens out with increasing u in proportion to the decrease in volumetric growth (area inside thick lines).

3.1.3 VI - Deposition

From equation (8):

$$\frac{d(V/\delta A)}{dt} = V_p n_{sat} c$$

For stable state growth, the rate of change in the surface in the direction of growth must be everywhere equal to the beam speed v_b.

$$\frac{d\vec{r}}{dt} = \frac{dy}{dt}\,\hat{y} = v_b \hat{y} \tag{14}$$

We know from Deserno [11] that a constant surface variation $\delta\vec{r}$ leads to a volume variation of simply

$$\delta V = \delta\vec{r} \cdot (\vec{r}_u \times \vec{r}_w). \tag{15}$$

Turning the variations into time derivatives (with $\frac{d\vec{r}_u}{dt} = \frac{d\vec{r}_w}{dt} = 0$ since the surface shape is invariant and with $\vec{r}_u \times \vec{r}_w = \delta A\,\vec{N}$):

$$\frac{d(V/\delta A)}{dt} = \frac{d\vec{r}}{dt} \cdot \vec{N} = v_b(\hat{y} \cdot \vec{N}) \tag{16}$$

where $\hat{y} \cdot \vec{N} = \frac{x_u z_w - x_w z_u}{\sqrt{x_w^2 + y_w^2 + z_w^2}}$ is the y-component of the normal. And thus we have the growth constraint:

$$\hat{y} \cdot \vec{N} = \frac{V_p n_{sat} c}{v_b} = \frac{n_{sat}}{\alpha} c \tag{17}$$

where α [prec./nm^2/ms] is the precursor decomposition rate density required at the tip to for the growth to keep pace with beam movement.

3.1.4 VII - SE production (and III - Decomposition)

The SE flux experienced on the perpendicular cross-section surface is only dependent on the distance from the beam, so it can be written as a function of $r = |\vec{r}| = \sqrt{x(u)^2 + y(u)^2}$. When calculating w-derivatives the flux may also depend on z.

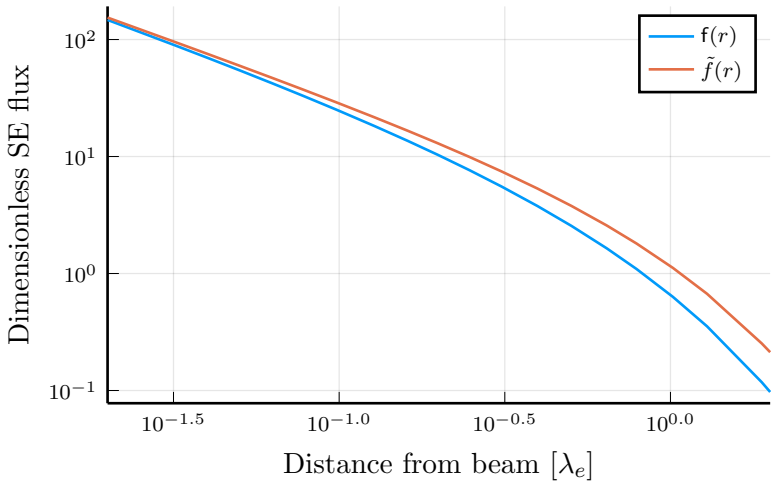

Figure 6: Strength of the dimensionless SE flux at the surface as a function of distance from the beam. Also shown is the approximation $\tilde{f}(r) = e^{-r}\frac{\pi}{r}$.

The perpendicular cross-section has smaller pillar width than the parallel[3], so we can approximate the SE source as an infinite line (exponential decay even reduces the error from this approximation). This also makes f independent of z.

$$f_{SE}(r) = \frac{I}{q_e} N_{SE} \int_{\mathcal{B}} e^{-\frac{r'}{\lambda_e}} \frac{1}{r'^2}\, db \approx \frac{I}{q_e} N_{SE} \int_{-\infty}^{\infty} e^{-\frac{r'}{\lambda_e}} \frac{1}{r'^2}\, db, \tag{18}$$

$$\text{with } r' = \sqrt{r^2 + b^2}$$

We can remove the dependency on λ_e from the flux equation by substituting $R = r/\lambda_e$ and $B = b/\lambda_e$. We then have $R' = \sqrt{R^2 + B^2} = r'/\lambda_e$. Since the integration is unlimited, there is no change in the integration bounds.

$$f_{SE}(r) = \frac{I}{q_e} N_{SE} \int_{-\infty}^{\infty} e^{-R'} \frac{1}{(\lambda_e R')^2}\, d(\lambda_e B) = \frac{I N_{SE}}{q_e \lambda_e} \mathsf{f}(R) = \frac{I N_{SE}}{q_e \lambda_e} \mathsf{f}(\frac{r}{\lambda_e}) \tag{19}$$

where

$$\mathsf{f}(R) = \int_{-\infty}^{\infty} e^{-R'} \frac{1}{R'^2}\, dB. \tag{20}$$

Inserting the above results for the SE flux into equation 5 for decomposition rate, we have

$$c = \sigma^{eff} \frac{I N_{SE}}{q_e \lambda_e} \mathsf{f}(r/\lambda_e) n = \frac{\beta}{\lambda_e} \mathsf{f}(r/\lambda_e) n. \tag{21}$$

where β scales the decomposition rate due to the SE flux from the ion beam and has the units of $[\frac{\text{decompositions}}{\text{precursors}} \frac{m}{s}]$.

4 Derivation of the ODE with angular surface diffusion

The differential equation describing the rate of change in precursor coverage is the sum of the m terms I, II, and III

$$\frac{\partial n}{\partial t} = D \nabla_S^2 n + \frac{\gamma}{n_{sat}} (1 - n) - c. \tag{22}$$

[3]This is simply due to the parallel cross-section experiencing more flux on the sides near the beam entrance and exit.

The growth restriction (constant vertical growth over the whole surface) is

$$\vec{N} \cdot \hat{y} = \frac{n_{sat}}{\alpha} c \tag{23}$$

where c is the decomposition rate

$$c = \frac{\beta}{\lambda_e} \mathsf{f}(r/\lambda_e) n, \tag{24}$$

$\vec{N} \cdot \hat{y} = \frac{x_u z_w - x_w z_u}{\sqrt{x_w^2 + y_w^2 + z_w^2}}$ is the y-component of the normal, $r = \sqrt{x^2 + y^2}$ is the distance to the ion beam, and $\alpha, \beta, \gamma, D, n_{sat}, \lambda_e$ are constants.

4.1 On the cross-section

Our first step is to evaluate equations 22 and 23 on the cross-section $w = 0$ to find an ODE we can integrate to find the stable state ($n_t = 0$) shape of the surface on that cross-section.

Expanding the Laplace-Beltrami operator as in equation 12:

$$\begin{aligned} m_{\mathrm{I}} &= D \nabla_S^2 n \\ &= \frac{D}{\sqrt{g}} \left((\sqrt{g} n_u)_u + (\sqrt{g} g^{22} n_w)_w \right) \\ &= D \left(n_{uu} + \frac{\sqrt{g}_u}{\sqrt{g}} n_u + \frac{1}{\sqrt{g}^2} n_{ww} - \frac{\sqrt{g}_w}{\sqrt{g}^2} n_w \right) \end{aligned} \tag{25}$$

Where we had for this coordinate system $\sqrt{g} = \sqrt{x_w^2 + y_w^2 + z_w^2}$ and $g^{22} = \frac{1}{\sqrt{g}^2}$.

Evaluating the equation on the cross-section means that the mirror symmetry can be applied. As stated before, symmetry dictates that odd-ordered w-derivatives of x, y, n and their u-derivatives are zero, and even-ordered w-derivatives of z and its u-derivatives are zero. Applying this mirror symmetry at $w = 0$, we get

$$m_{\mathrm{I}}/D = \nabla_S^2 n = n_{uu} + \frac{z_{uw}}{z_w} n_u + \frac{1}{z_w^2} n_{ww} = \frac{(z_w n_u)_u}{z_w} + \frac{1}{z_w^2} n_{ww} \tag{26}$$

We merged the n_{uu} and n_u terms into one to avoid having to explicitly calculate n_{uu} in the first step of integration.

Filling in this result in equation 22, setting $n_t = 0$, and evaluating at $w = 0$ gives us an partial differential equation for precursor density:

$$(z_w n_u)_u = \frac{z_w}{D} \left(c - \frac{\gamma}{n_{sat}} (1 - n) \right) - \frac{1}{z_w} n_{ww} \tag{27}$$

And evaluating equation 23 at $w = 0$ gives a differential equation for x depending only on x and y:

$$x_u = \frac{n_{sat}}{\alpha} \tag{28}$$

An equation for the value of y can be found via the arc-length constraint:

$$y_u = \sqrt{1 - x_u^2} \tag{29}$$

The above three equations give us an ODE system that can be numerically integrated to find the shape of the cross-section x, y, and the precursor density n. Unfortunately the equation for n requires us to know the angular derivatives z_w and n_{ww}, so we will derive their formulae in the next section.

4.2 Deriving formulae for the angular variables

In the previous section we evaluated equations 22, 23 and the arc-length constraint within the cross-section $z = w = 0$. To retrieve an estimate about the diffusion that occurs perpendicularly to this cross-section, we look at the w-derivatives in this cross-section, akin to higher order Taylor series terms.

As will be shown shortly, to calculate z_{uw} we need information about the curvature in the form of x_{ww} and y_{ww}, so formulae for x_{uww} and y_{uww} will be needed as well. The formula for $(z_w n_{uww})_u$ includes z_{uwww} and z_{www}, so similarly we will need x_{uwwww} and y_{uwwww}.

The derivations that follow were assisted by the symbolic mathematics package SymPy in Julia, and double-checked by hand derivation.

First we use the orthogonality of the parameterisation $\boldsymbol{e}_u \cdot \boldsymbol{e}_w = x_u x_w + y_u y_w + z_u z_w = 0$, take the first and third derivative to w, and evaluate at $w = 0$ to find:

$$z_{uw} = -\frac{1}{z_w}(x_u x_{ww} + y_u y_{ww}) \tag{30}$$

$$z_{uwww} = -\frac{1}{z_w}(x_u x_{wwww} + 3x_{uww}x_{ww} + y_u y_{wwww} + 3y_{uww}y_{ww} + 3z_{uw}z_{www}) \tag{31}$$

Second, we take the second and fourth derivative to w of the growth constraint (equation 23) to find:

$$x_{uww} = \frac{n_{sat}}{\alpha}c_{ww} + (x_{ww}^2 + y_{ww}^2)\frac{x_u}{z_w^2} + 2x_{ww}\frac{z_{uw}}{z_w} \tag{32}$$

$$\begin{aligned} x_{uwwww} = &\frac{n_{sat}}{\alpha}c_{wwww} + 4\left(x_{ww}z_{uwww} + x_{wwww}z_{uw}\right)\frac{1}{z_w} \\ &- 9\left(x_{ww}^2 + y_{ww}^2\right)^2 x_u\frac{1}{z_w^4} - 12(x_u z_{www} + x_{ww}z_{uw})(x_{ww}^2 + y_{ww}^2)\frac{1}{z_w^3} \\ &+ 2(+2x_u x_{wwww} + 3x_{ww}x_{uww} - 6z_{www}z_{uw})x_{ww}\frac{1}{z_w^2} + 2(2x_u y_{wwww} + 3y_{ww}x_{uww})y_{ww}\frac{1}{z_w^2} \end{aligned} \tag{33}$$

Note that the z_{www} term in the first equation and the z_{wwwww} term in the second equation both cancel out to zero.

Third, we use the arc-length constraint $\boldsymbol{e}_u \cdot \boldsymbol{e}_u = x_u^2 + y_u^2 + z_u^2 = 1$ and take the second and fourth derivative to w:

$$y_{uww} = -\frac{1}{y_u}(z_{uw}^2 + x_u x_{uww}) \tag{34}$$

$$y_{uwwww} = -\frac{1}{y_u}(x_u x_{uwwww} + 3x_{uww}^2 + 3y_{uww}^2 + 4z_{uw}z_{uwww}) \tag{35}$$

Finally, if we take the second derivative to w of equation 22 (with $n_t = 0$):

$$\begin{aligned} (z_w n_{uww})_u = &\frac{z_w}{D}\left(c_{ww} + \frac{\gamma}{n_{sat}}n_{ww}\right) + 4\left((x_{ww}^2 + y_{ww}^2)\frac{1}{z_w} + z_{www}\right)\frac{1}{z_w^2}n_{ww} \\ &+ \left(2(x_{ww}^2 + y_{ww}^2)\frac{z_{uw}}{z_w} - 2x_{ww}x_{uww} - 2y_{ww}y_{uww} + z_{uw}z_{www} - z_w z_{uwww}\right)\frac{1}{z_w}n_u \\ &- \frac{1}{z_w}n_{wwww} \end{aligned} \tag{36}$$

We can repeat this process to find an equation for n_{uuwwww}, but this would be endless so instead we derive an estimate through the following: Given a slice of the surface for some constant y value, we assume the intersection with the surface to be roughly elliptical, such that $z = C_1(y)\sin\theta$ (where θ is the angular parameterisation of the ellipse, C_i indicate arbitrary functions). Since n_{uu} has some local minima/maxima at the points $\theta \in \{0, \pi/2, \pi, 3\pi/2\}$ due to reflective symmetry at these points, we assume n_{uu} is roughly (co-)sinusoidal with respect to θ such that $n_{uu} = C_2(y) + C_3(y)\cos(2\theta)$. Using the identity $\cos(2\arcsin(\cdot)) = 1 - 2(\cdot)^2$, we find

$$n_{uu} = C_4(y) + C_5(y)z^2$$

and thus $\frac{\partial^4 n_{uu}}{\partial z^4} = 0$. Using this result–and arbitrarily neglecting higher order u-derivatives[4] of n–we find by the chain rule for partial derivatives:

$$n_{uuwwww} = \left(4\frac{z_{www}}{z_w} - 12\frac{y_{ww}z_{uw}}{y_u z_w}\right) n_{uuww}$$

Since for $u = 0$ we have $n_{ww} = n_{uww} = n_{wwww} = n_{uwwww} = 0$, in general

$$n_{wwww}(u, w) = \left(4\frac{z_{www}}{z_w} - 12\frac{y_{ww}z_{uw}}{y_u z_w}\right) n_{ww}. \tag{37}$$

With the addition of the above equations, we now have a complete and integrable ODE system:

[4]When including the higher order u-derivatives and inserting them into the equation for $(z_w n_{uww})_u$, the equation becomes higher order, leading to inaccuracies when using it merely to calculate an estimate. It may be possible to rearrange the equation to become a calculation for n_{uuuu}, but this leads to more unsolved complexity–for example in the calculation of y_{uu}, and in determining the initial values of y_{uu} and n_{uu}. A minor validation for the resulting estimate of n_{wwww} is that it leads to a factor of n_{ww} which has the correct sign to allow solutions with the expected asymptotic behaviour for $u \to \infty$ (zero diffusion).

$$
\begin{aligned}
x_u &= \frac{n_{sat}}{\alpha} c \\
x_{uww} &= \frac{n_{sat}}{\alpha} c_{ww} + (x_{ww}^2 + y_{ww}^2)\frac{x_u}{z_w^2} + 2x_{ww}\frac{z_{uw}}{z_w} \\
x_{uwwww} &= \frac{n_{sat}}{\alpha} c_{wwww} + 4\left(x_{ww} z_{uwww} + x_{wwww} z_{uw}\right)\frac{1}{z_w} \\
&\quad - 9\left(x_{ww}^2 + y_{ww}^2\right)^2 x_u \frac{1}{z_w^4} - 12(x_u z_{www} + x_{ww} z_{uw})(x_{ww}^2 + y_{ww}^2)\frac{1}{z_w^3} \\
&\quad + (4x_u x_{wwww} + 6x_{ww}x_{uww} - 12 z_{www} z_{uw}) x_{ww}\frac{1}{z_w^2} + (4x_u y_{wwww} + 6y_{ww}x_{uww}) y_{ww}\frac{1}{z_w^2} \\
y_u &= \sqrt{1 - x_u^2} \\
y_{uww} &= -(z_{uw}^2 + x_u x_{uww})/y_u \\
y_{uwwww} &= -\frac{1}{y_u}(x_u x_{uwwww} + 3x_{uww}^2 + 3y_{uww}^2 + 4 z_{uw} z_{uwww}) \\
z_{uw} &= -\frac{1}{z_w}(x_u x_{ww} + y_u y_{ww}) \\
z_{uwww} &= -\frac{1}{z_w}(x_u x_{wwww} + 3x_{ww}x_{uww} + y_u y_{wwww} + 3y_{ww}y_{uww} + 3z_{uw}z_{www}) \\
(z_w n_u)_u &= \frac{z_w}{D}\left(c - \frac{\gamma}{n_{sat}}(1-n)\right) - \frac{1}{z_w} n_{ww} \\
(z_w n_{uww})_u &= \frac{z_w}{D}\left(c_{ww} + \frac{\gamma}{n_{sat}} n_{ww}\right) + 4\left((x_{ww}^2 + y_{ww}^2)\frac{1}{z_w} + z_{www}\right)\frac{1}{z_w^2} n_{ww} \\
&\quad + \left(2(x_{ww}^2 + y_{ww}^2)\frac{z_{uw}}{z_w} - 2x_{ww}x_{uww} - 2y_{ww}y_{uww} + z_{uw}z_{www} - z_w z_{uwww}\right)\frac{1}{z_w} n_u \\
&\quad - \left(4\frac{z_{www}}{z_w^2} - 12\frac{y_{ww}z_{uw}}{y_u z_w^2}\right) n_{uuww}
\end{aligned}
$$

with

$$
\begin{aligned}
r &= \sqrt{x^2 + y^2} \\
r_{ww} &= (x x_{ww} + y y_{ww})/r \\
r_{wwww} &= (x x_{wwww} + 3x_{ww}^2 + y y_{wwww} + 3y_{ww}^2 - 3r_{ww}^2)/r \\
\mathsf{f} &= \mathsf{f}(r/\lambda_e, z = 0) \\
\mathsf{f}_{ww} &= r_{ww}\mathsf{f}_r + z_w^2 \mathsf{f}_{zz} \\
\mathsf{f}_{wwww} &= 3r_{ww}^2 \mathsf{f}_{rr} + 4 r_{ww} z_w^2 \mathsf{f}_{rzz} + r_{wwww}\mathsf{f}_r + z_w^4 \mathsf{f}_{zzzz} + 4 z_w z_{www}\mathsf{f}_{zz} \\
c &= \frac{\beta}{\lambda_e}\mathsf{f} n \\
c_{ww} &= \frac{\beta}{\lambda_e}(\mathsf{f}_{ww} n + \mathsf{f} n_{ww}) \\
c_{wwww} &= \frac{\beta}{\lambda_e}(\mathsf{f}_{wwww} n + 6\mathsf{f}_{ww} n_{ww} + 4\frac{z_{www}}{z_w}\mathsf{f} n_{ww})
\end{aligned}
$$

Putting the above in simple terms, the slope of x (which determines the width of the pillar) depends on the amount of decomposition c (via the steady-state assumption). y_u is related to x_u simply such that the arc-length parameterisation holds. z_w is kept such that the orthogonality between u and w is maintained. Finally, n is determined by the amount of decomposition and diffusion. For each of these there are then also the higher order w-derivative equivalents.

Note that the z-derivatives of f are also written down, but they are equal to zero while the assumption that the beam SE generation length is infinite is in place.

4.3 Initial conditions

The initial conditions (at $u = 0$) are:

$$\begin{aligned} x &= 0 & y &= r_0 \\ n &= n_0 & (z_w n_u) &= 0 \\ z_w &= 0 & & \\ x_{ww} &= 0 & y_{ww} &= 0 \\ n_{ww} &= 0 & (z_w n_{uww}) &= 0 \end{aligned}$$

Using the symmetry condition that $x_u(u = 0) = 1$, we can calculate a value for r_0 from some initial n_0:

$$r_0 = \frac{\lambda_e}{n_0} \mathsf{f}^{-1}\left(\frac{\alpha \lambda_e}{\beta n_{sat}}\right) \tag{38}$$

where f^{-1} is the inverse (unitless) SE flux. The function f has no closed form, so we cannot derive one for its inverse, but $\mathsf{f}^{-1}(f)$ can be found numerically by finding the root of $\mathsf{f}(\cdot) - f$. We use an approximation of the inverse of f in a root-finding algorithm to find the true inverse. This is to ensure more reliable convergence. We run the root-finding algorithm on the function $\tilde{\mathsf{f}}^{-1}(\mathsf{f}(\cdot))$:

$$\tilde{\mathsf{f}}^{-1}(\mathsf{f}(\cdot)) - \tilde{\mathsf{f}}^{-1}(f) \to 0$$

with an initial estimate of

$$\tilde{\mathsf{f}}^{-1}(f)$$

where

$$\tilde{\mathsf{f}}^{-1}(f) = W_0\left(\frac{\pi}{f}\right)$$

where W_0 is (the principal branch of) the Lambert W function, the inverse of $x \to xe^x$. This approximation is based on $(r) \approx e^{-r\frac{\pi}{r}}$ which is obtained by moving the exponential term outside of the integral[5].

During the first integration step, the second half of the formulae in the ODE system contain division by $z_w = 0$, so we use a polar parameterisation that holds near the origin, trivial from the definition of the geodesic polar parameterisation

$$\vec{r}(u, w) = \begin{bmatrix} \cos(w)u + \mathcal{O}(u^3) \\ r_0 + \mathcal{O}(u^2) \\ \sin(w)u + \mathcal{O}(u^3) \end{bmatrix} \tag{39}$$

Limit evaluation of the parameterisation then gives the following results.

$$\begin{aligned} x_u(0,0) &= 1 & x_{uww}(0,0) &= -1 & x_{uwwww}(0,0) &= 1 \\ y_u(0,0) &= 0 & y_{uww}(0,0) &= 0 & y_{uwwww}(0,0) &= 0 \\ z_{uw}(0,0) &= 1 & z_{uwww}(0,0) &= -1 & & \\ (z_w n_u)_u(0,0) &= 0 & (z_w n_{uww})_u(0,0) &= 0 & & \end{aligned}$$

Note that we have no direct way of calculating the initial values of n_{uu} and n_{uuww}, which is why the equations for $(z_w n_u)_u$ and $(z_w n_{uww})_u$ are used in the ODE system instead.

[5]The definite integral of $1/(r^2 + x^2)$ over x is evaluated as π/r

D	540 (?)	nm^2/ms
n_{sat}	1.9 ±0.5	$/nm^2$
α	0.56–11.1 ± (0.12–2.5)	$/nm^2/ms$
v_b	0.05–1.00	nm/ms
V_p	0.09 ±0.02	nm^3
β	0.83 ±0.18	nm decomp./prec./ms
I	0.35 ±0.05	pA
N_{SE}	0.32	SE/ion/nm
q_e	1.602×10^{-4}	fC/ion
σ^{eff}	$1.2 \pm 0.2 \times 10^{-3}$	nm^2 decomp./prec./SE
γ	0.0102 ±0.0035	prec./nm^2/ms
f_p	0.32 ±0.11	prec./nm^2/ms
s	0.1 (?)	
λ_e	1.5 (0.8–6.0)	nm

Table 1: Ranges and values of parameters and constants as as relevant to the experiment of [1]. Uncertainties are approximate. Question marks (?) indicate that the uncertainty is significant but unknown.

4.4 Physical constants and operational parameters

The equations derived for the model has 6 independent constants/parameters: $D, n_{sat}, \alpha, \beta, \gamma, \lambda_e$, where α, β, γ are multiplicative combinations of various constants/parameters. To compare the results of our model with the experiments of [1], we need to use the same values for operational parameters (precursor type, beam speed, beam current, precursor flux). We also need to determine values for physical constants from literature.

The results of this section may be found in table 1.

4.4.1 Diffusion constant D

The diffusion constant for precursor gases at room temperature are estimated to be on the order of 100 nm^2/ms for use in simulation [12] [13]. The precursor MeCpPtMe3 has been calculated to have a diffusion coefficient of 540 nm^2/ms based on fits to empirical measurements of IBID pillar growth with a pulsed beam [4].

4.4.2 Precursor saturation density n_{sat}

In [6] n_{sat} for MeCpPtMe3 is given as 1.9 /nm^2. This value is calculated using "the maximum bond length of the molecule from crystallographic data". The uncertainty in this method "can differ within several tens of percent for the same molecule according to its geometric configuration", and thus we approximate an uncertainty of 0.5 /nm^2.

4.4.3 Beam speed v_b

[1] uses a 1 nm beam step size and varied the beam dwell time between 1 and 20 ms. This range in dwell times leads to a v_b range of average speeds 0.05–1 nm/ms.

4.4.4 Deposition volume V_p

V_p is given as 0.091 nm^3 per Pt atom in [4], which cites the value for PtC_4 density (11 /nm^3) from [14]. (This seems to assume that on average 1 Pt and 4 C is deposited per decomposition.) This PtC_4 density is in turn based on the mass density with 11% uncertainty calculated in [15] via cantilever experiments. However this mass density was for a deposition of an estimated 15% platinum deposit (made with FEB), as opposed to 20%; there some more uncertainty in the value due to our uncertainty of the Pt:C ratio of the deposit. And so we take $V_p = 0.09 \pm 0.02$ nm^3.

4.4.5 Beam current I

The experiments in [1] uses $0.35 \pm .05$ pA (a very low setting). For investigating the precursor-limited regime, we may want to use a higher value–likely still below 10 pA.

4.4.6 SE production rate N_{SE}

[14] uses a secondary electron coefficient of 2.9 (SEs per ion) for a flat Pt20C80 substrate, which is allegedly equal to that of pure Pt and pure C. This value is based on the results of [16]. However, this is the value stated for a 25 keV beam (1.1×10^6 m/s). The experiments in [1] used a 30 keV beam (1.2×10^6 m/s), which according to [16] means a SE coefficient of 3.0. This SE coefficient is the number of SEs that exit the substrate when the beam is fired straight into a flat surface. We call this coefficient $N_\perp$.

However, we need N_{SE}, which we defined as the number of SEs that are emitted isotropically from the ion path per unit distance.

The number of SEs generated per unit distance N_{SE} can be calculated from the secondary electron coefficient for a flat Pt20C80 substrate $N_\perp$ by calculating the integral of the flux over a flat surface (for a beam perpendicular to the surface). The flux function f is divided by 2 here since it normally integrates from $-\infty$ to ∞.

$$N_\perp = \frac{N_{SE}}{\lambda_e} \int_0^\infty 2\pi r \frac{\mathsf{f}(r/\lambda_e)}{2}\, dr = 2\pi\lambda_e N_{SE}. \tag{40}$$

The equation is simplified by using the result $\int_0^\infty \int_0^\infty e^{-\sqrt{(ar)^2+b^2}} \frac{r}{(ar)^2+b^2}\, dr\, db = \frac{1}{a^2}$. Thus we have simply $N_{SE} = \frac{N_\perp}{2\pi\lambda_e} = 0.32$ SE/ion/nm.

4.4.7 Elementary charge q_e

The elementary charge $q_e \approx 1.602 \times 10^{-4}$ fC is assumed to be common knowledge.

4.4.8 Effective decomposition cross-section σ^{eff}

The electron-precursor cross-section depends highly on the energy of the electron. [17] has empirically determined values for the MeCpPtMe3 precursor cross-section ranging over 3–3000 eV.

The energy distribution of SEs due to excitation by a He-ion beam may be seen in [18] and [14].[6] The distribution peaks around 1 eV and has a thick tail going to 6 eV, which then drops off to nothing after 11 eV. Visually taking the product between this N_{SE} distribution and the cross-section as a function of energy, we find an approximately flat distribution between 3-8 eV that is close to zero everywhere else.

In this range the cross-section is approximately equal to $4.2 \pm 0.3 \times 10^{-3}$ nm^2 (the value stated for 8 eV). Since not all SEs have a significant cross-section, we multiply by the fraction of SEs produced in the range 3-8 eV: about 0.8/2.9 based on the bar graph of [14].

In total this gives $\sigma^{eff} = 1.2 \pm 0.2 \times 10^{-3}$ nm^2.

4.4.9 Precursor flux f_p

In the experiments of [1] they use a nozzle with a 500 μm wide opening positioned around 150-200 μm above the substrate, at an angle of 25°. The calculations of [19] gives a precursor flux at the nozzle tip of 1.72 molecules /nm^2/ms under similar conditions (precursor reservoir at room temperature and background pressure around 5×10^{-7} mbar); only the diameter is 500 μm instead of 400 μm.[7] In accordance with these calculations, the flux at the nozzle tip is proportional to the diameter, so 2.15 /nm^2/ms for our case.

The flux at the deposition site should be 5-10 times lower than the at the tip [19]. So we have an approximate value of $f_p = 0.32 \pm 0.11$/nm^2/ms.

4.4.10 Precursor sticking coefficient s

[14] cites a sticking coefficient of 0.1, but mentions that it has a high uncertainty. The citation is of [6], but I could not find a value given in the citation.

[9] also cites a value of 0.1 from [12], but its references for this value are not reliable: The first simply assumes 0.1 for an order of magnitude calculation (in the context of adsorption to SiN rather than amorphous PtCx), and the second is a calculated value for Pt during physical vapour deposition.

Unfortunately this means that the best we have to go off of is that assuming 0.1 for the sticking coefficient is the precedent.

4.4.11 Electron inelastic mean free path λ_e

There seems to be no clear consensus yet in the accurate measurement of the IMFP (inelastic mean free path) of low energy electrons (<100 eV) [20] [21] [22] [23] [24].

The IMFP also has a strong sensitivity to energy at low energies. 4eV electrons can have 4 times higher IMFP than 8eV due to IMFP being roughly proportional to $\frac{1}{\text{energy}^2}$ at low energies [25].

[20] gives approximately $\lambda_e = 1.5$ nm in elemntal Pt for an electron with 6 eV of energy remaining in vacuum. No data could be found specifically for IMFP in PtCx compounds.

[6] We do not take into account that electron penetration depth depends on energy when considering the distributions.

[7] [19] also uses an angle of 34° which allows the beam access to more the more concentrated part of the impingement, but further away from the surface at 450 μm.

If we assume for PtCx that we also have $\lambda_e(6\text{eV}) = 1.5$ nm, given our energy range 3–8 eV–and the inverse square dependence on energy–we get an IMFP in the range $\lambda_e \in 0.8$–6.0 nm. If we assume the SE energy distribution (weighted by cross-section) is flat, the higher λ_e values in this range is rarer due to the inverse square relationship with energy, and so we take an 'average' value as $\lambda_e = 1.5$ nm.

4.5 Numerical methods

For our numerical calculations, we use the Julia language [26], which boasts the ease of use of a dynamic language like Python combined with the computation speed of low level languages like C.

4.5.1 ODE solver

We use the "performant and feature-rich ecosystem for solving differential equations in Julia" package called DifferentialEquations.jl [27].

Since the ODE system includes many divisions by variables that go to 0 as $u \to 0$, there is some potential for instability. To avoid this, we first make 20 integration steps (of size `1e-4`$*r_0$) using the `RK064` solver as provided by the package. `RK065` is Tsitouras' Runge-Kutta-Oliver 6 stage 5th order method, which has been developed to be robust on problems which have a singularity at the initial value [28].

Unfortunately, this solver has not yet been implemented to allow for adaptive timestepping, so to speed up the solution, another solver is used after this initial integration. For the second integration, we use the `BS5` solver as supplied by DifferentialEquations.jl with relative tolerance specified as `1-e8`. `BS5` is one of the solvers recommended for non-stiff problems and uses the Bogacki-Shampine 5/4 Runge-Kutta method [29].

The solver is stopped once the precursor coverage goes below 0 or above 1.

4.5.2 Flux approximation

The (unit-less) SE flux integral of equation 20 was implemented to be calculated by `quadgk` from QuadGK.jl [30] with a relative tolerance of `1e-10`.

The first and second order derivatives were implemented using forward-mode automatic differentiation via ForwardDiff.jl [31].

These functions take around 17–26 μs to evaluate, and take up the majority of the computation time when used in the numerical integration steps.

To speed up these function evaluations, we use ApproxFun.jl [32], which can actually be used for spectral solving of differential equation systems, but for now we are just using the approximation of functions as Chebyshev polynomials functionality.

We calculate the approximations by finding a piece-wise polynomials that approximate the logarithms of the functions, and exponentiating when evaluating. The logarithms are used because the flux function has a singularity, and has a range over many orders of magnitude. The logarithms and the splitting up of the domain achieves a greater accuracy across the full domain using less terms than just using one polynomial to represent the whole function.

The relative error introduced by these approximations is less than 10^{-13}—less than that of the numerical integration. These approximations take around 550 ns to evaluate: a speed-up of 40

times! This leads to faster ODE solving, which in turn allows for real-time viewing of results and tweaking of calculations.

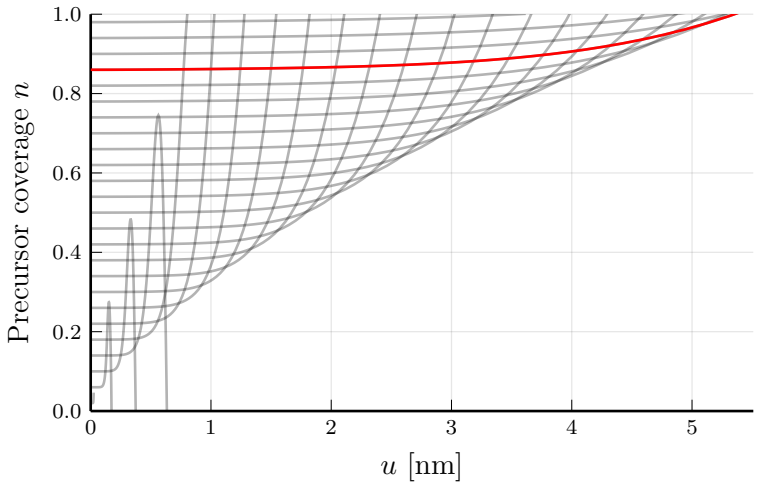

Figure 7: The precursor coverage over the arc-length u for different starting values of $n(u = 0)$. The red line is of the solution corresponding to the longest pillar. It has $n(u = 0) = 0.86$.

5 Results

In the results section we will heavily compare with the pillar width measurements of the experiments carried out in [1] by G. Nanda et al. The authors identified three regimes separated by different beam dwell times (resulting in different speeds). From the paper:

> Three regimes can be distinguished in the plot of the needle volume per ion versus dwell time: (1) the nucleation regime (0-4 ms in Fig. 3) where no significant growth takes place; (2) an intermediate regime (4-8 ms) characterized by a fast increase of the needle volume per ion; (3) and the saturation regime (beyond 12 ms) where the needle volume per ion attains a more or less constant value

The latter two is referred to in [4] as the ion-limited regime and the precursor-limited regime, respectively.

5.1 Short dwell time

We start with the lowest dwell time (i.e. the fastest beam speed) used in the experiment, 1 ms ($\alpha = 11.11$ /nm^2/ms). Using the parameters in table 1, we solve the ODE for various initial values of n. The precursor coverage $n(u)$ of these solutions (over the arc-length u) is shown in figure 7.

Our model requires infinite pillars for the assumptions of constant precursor coverage ($n_t = 0$) and growth equalling beam speed to be appropriate. Since the solutions presented in figure 7 have precursor coverage values that depart the physical range between 0 and 1 within a finite u value, there seems to be no steady-state solutions with this set of parameters.

It is tempting to interpret these solutions as shorter pillars that are limited in growth, but pillars that are undergoing changes due to growth are not reconcilable with the restrictions we have added: Real solutions would have the precursor coverage on the pillar to be decreasing as it grows, since the diffusion source (base) keeps getting further away (hence $n_t \neq 0$). If a pillar cannot be grown beyond a certain length, it is because the growth cannot keep up with the speed of the beam (hence growth $<$ beam speed). Thus we cannot read much into the exact

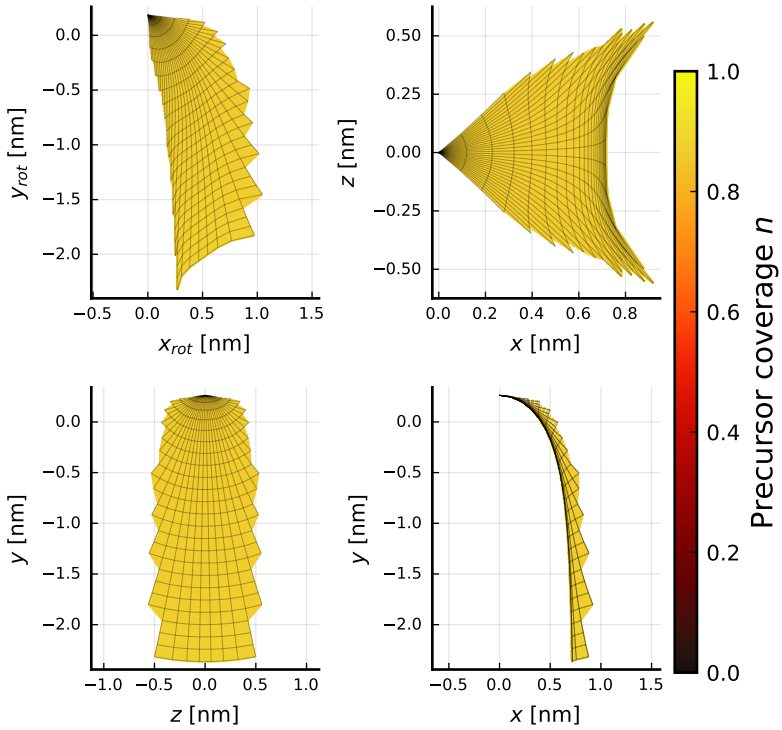

Figure 8: Short dwell time (1 ms) solution. The curves are generated through Taylor approximation along the cross-section $w = 0$ via the partial derivatives. This may be seen as an estimate of the local shape and precursor distribution. x_{rot} and y_{rot} shows the surface after being rotated $\pi/4$ around the x-axis and $-\pi/4$ around the y-axis.

characteristics of these solutions, except that in some way, the longer they are, the closer they are to a real steady-state solution.

It is expected that this fast beam speed (dwell time of 1 ms) outpaces any significant growth. This lack of long solutions may be what was referred to as the nucleation regime, found by [1] to be with a dwell time in the range of 0–4 ms.

The precursor coverage of some solutions have sharp peaks followed by a rapid descent. That the solutions don't reach saturation indicates that these low precursor coverage values cannot be attained by having a saturated diffusion source at the base of the pillar. The presence of such solutions are somewhat expected. However, it is unusual that the solutions show a very constant coverage followed by a steep ascent. Whereas we expect a depleted tip (due to SE decomposition) followed by a gradual increase in coverage (due to adsorption effects), indicating further that these solutions are not realistic.

Figure 8 shows the shape of the surface close to the $w = 0$ cross-section of the longest solution in figure 7 (shown with the red line). The x-y-z positions were calculated for an array of u and w values by interpolating the solution for the u values, and using the w-derivatives as Taylor coefficients for the w values.

The monotone colour indicates that it has a precursor coverage that does not vary significantly. This is especially notable on the curved part of the tip, since we would expect depletion there. This is a strong indication that this solution is in the precursor-limited regime (as expected for a high beam speed).

The shape along the $w = z = 0$ cross-section is as one would expect for the pillar shape: a round tip with a asymptotically vertical wall further away. This can easily seen on the bottom right

x-y subplot.

However, we find that the pillar is unrealistically thin with a diameter of 1.5 nm, much less than the smallest needle achieved of 13 nm. With such a small dwell time, the growth volume is similarly small, and thus a very thin pillar is theoretically needed for the growth to keep up with the beam speed. It may be possible that such a small pillar would be possible under more ideal circumstances of infinitely thin ion beam and vibration-less motion, but for now we should remember that this solution is still not valid due to assumptions that require infinite pillar length.

The surface appears very flat close to the $z = 0$ cross-section, as can be seen in the two right-hand subplots. The surface has apparently zero Gaussian curvature around the $w = 0$ cross-section. Further away (higher z values) it does start curving due to the fourth derivative eventually overwhelming, but this may well be due to the inaccuracy of Taylor approximations. This low (and even outwards) curvature indicates that the solution is not really pillar-like. In the numerical solving, there is an assumption baked in that $y_u(w = 0)$ is negative, so the surface will always be curving downwards along $w = z = 0$. There is no such assumption for the z-direction, meaning that curving upwards in the z-direction is a technically valid solution, which can result in the tip being a saddle-point. With the outwards-curving surface, this seems to be the case with this solution.

5.2 Nucleation regime

For any given set of parameters, we can find the n_0 value that corresponds to the solution which has the longest the pillar. Figure 7 shows the solution of the longest pillar for that set of parameters as a red line. We use the `optimize` method[8] of the Optim.jl package over the bounds $n_0 \in [0.2, 0.995]$ with a low relative tolerance of `1e-4`. The low relative tolerance approximately halves the required function evaluations (each of which requires solving the ODE) to speed up calculation.

If we plot this maximal pillar length as a function of the parameters, we can see a distinct boundary between the regions where pillar solutions of unlimited length exist and where they don't. See figure 9.

For the experimental parameters, we found the boundary to be at $\alpha = 5.59\beta = 4.66$ /nm^2/ms, corresponding to the a dwell time of 2.4 ms. Dwell times larger than 2.4 ms have solutions with unlimited pillar length. According to this model then, the length of pillars grown in this regime are only limited by the duration of precursor and ion bombardment. This boundary value compares well with the experimental value of 4 ms, especially considering the level of uncertainty present.

Looking at the n_0 values of the maximal solutions, we can see high saturation, especially with such low values for β. When the precursor saturation is high, the only parameter[9] that affects the ODE is the unit-less $\frac{n_{sat}\beta}{\alpha\lambda_e}$. With the experimental parameter values the nucleation or growth regime is thus approximately

$$\frac{n_{sat}\beta}{\alpha\lambda_e} \gtrsim 0.227 \tag{41}$$

This boundary described by this inequality is a linear relationship between α and β, as can be seen in figure 9. The deviation from this linear boundary at higher β values is likely due to the lower precursor density, complicating the system by introducing diffusion and adsorption

[8] The default zeroth-order univariate solver is Brent's method.

[9] Excluding the physical constant λ_e, which also appears within the flux calculation.

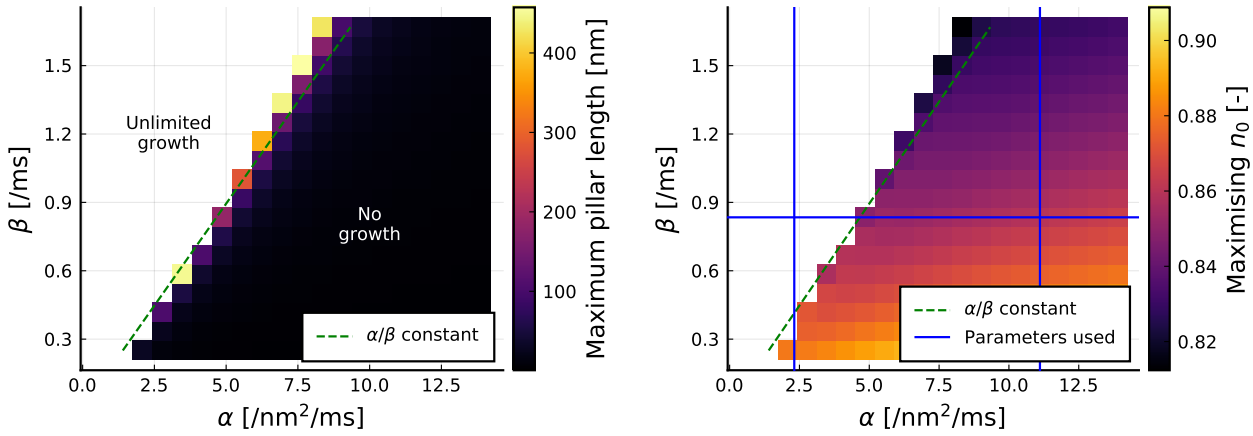

Figure 9: Points where the maximum pillar length is over 500 nm are left blank; due to the steep asymptotic behaviour, these points are at least very close to—or in—the nucleation regime. The dotted green line indicates the $\alpha = 5.59\beta$ boundary approximation. The blue lines indicate the values of α (proportional to beam speed) and β (proportional to ion current) that were investigated in the previous and following sections.

effects. Indeed, if the precursor density is lower, one would expect also that a higher ion dose (β) is needed for similar amounts of deposition and reliable growth.

5.3 Multiplicitous solutions

The experiments of [1] found a nucleation boundary at 4 ms dwell time and a transition in two growth regimes around 8 ms. Considering our model predicts 2.4 ms for the nucleation boundary, we may expect the transition in growth regimes to be the same doubling of the nucleation boundary at 4.8 ms ($\alpha = 2.31$). We are looking for a qualitative difference in the sensitivity to α on either side of this value.

Figure 10 highlights two solutions with this higher dwell time: The small solution (with lower n) and the large solution (with higher n). These two solutions are the only two solutions with asymptotic behaviour of the precursor coverage towards 1. Rather than infinitely long pillars, a finite pillar with a precursor coverage of 1 near its base is more realistic. Realistic solutions like these may be found with n_0 values just above the large solution or just below the small solution.

Considering that the z-direction diffusion term is dominant, it appears that the depleted areas of beam ingress and egress are not properly accounted for in this model. The large solution is especially egregious in this sense, as the diffusion in the z-direction is very large (while we expect it to be negative due to the depleted areas on the sides).

We can see also that for $u = 0$ the two terms of the diffusion rates are equal. This indicates that $n_{uuww}(u = 0) = 0$, and is confirmed by seeing from the solution that $\lim_{u\to 0} \frac{n_{ww}}{u^2} = 0$. This turns out to be due to a problem with the neglecting of the higher order u-derivatives of n_{uu} in the assumption that n_{uu} is (co-)sinusoidal in the x–z plane (see equation 37). To see this, dividing by z_w and taking the limit $u \to 0$ of equation 36 (with application of L'Hôpital where appropriate) results in:

$$2n_{uuww} = \lim_{u\to 0} -\frac{n_{wwww}}{z_w^2} = \left(2 + 3\frac{y_{uuww}}{y_{uu}}\right) n_{uuww}$$

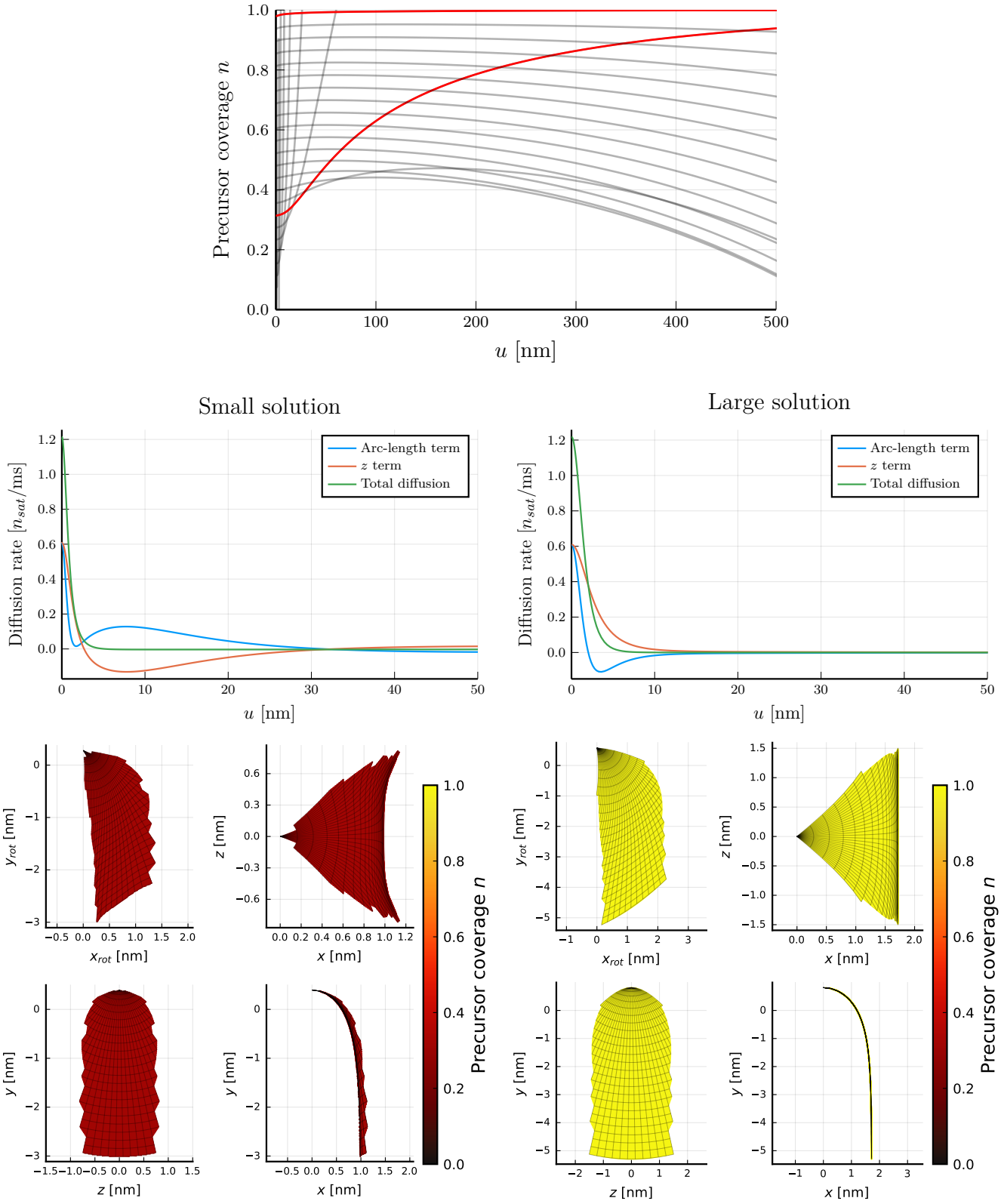

Figure 10: The two solutions with infinite pillar length at $\alpha = 2.31$. The initial precursor coverage of these solutions are $n_0 = 0.314$ and $n = 0.980$.

Which requires that either n_{uuww} or y_{uuww} is zero, and the latter is not zero due to the calculation of y_{uww}.

This shows that the assumption was too strong; the diffusion terms are not realistic, at least relative to each other.

The above problem is normally prevented by the fact that in the expanded chain rule formulation of $\frac{\partial^4 n_{uu}}{\partial z^4}$, the $-12\frac{y_{ww}z_{uw}}{y_u z_w}n_{uuww}$ term cancels with the $6\frac{y_{ww}}{y_u}n_{uuuww}$ term at $u = 0$. But as stated earlier, introducing this term (and other terms with higher order derivatives of n_{ww}) introduces too much complexity.

The simplest way of solving the problem at $u = 0$ is to use the assumption that $n_{uu} = C_a(u) + C_b(u)\cos(2w)$, which leads to $n_{wwww}(u, w) = 4\frac{z_{www}}{z_w}n_{ww}$. This assumption holds at $u = 0$, but quickly becomes less and less accurate as u increases and the geodesics start overlapping each other due to the pillar not being rotationally symmetrical, and thus we cannot reliably apply it to long pillars.

5.4 Sensitivity Analysis

Starting with the small solution, we look at how its characteristics vary when varying each parameter α, β, γ, λ, n_{sat} and D while holding the rest constant. Figure 11 shows the results of this.

The most striking result from figure 11 is that the pillar width increases with increasing beam speed (α) and also with decreasing ion dosage (β). This is highly unintuitive, since a larger amount of ions per unit distance over the length of the pillar should lead to more depositions and thus a wider pillar. The magnitude of the variation is very small compared to the variation observed in the experiment (which had a factor 6 variation in pillar width over a similar variation of beam speed). With just this we can judge that the small solution is not realistic.

The following figure 12 shows how the characteristics of the large solution changes due to varying parameters. We can see that this behaviour is much more intuitive compared to that of the small solution: The pillar width decreases with increasing beam speed and with decreasing ion dosage. The amount of variation is higher at a factor difference of roughly 2, but still much smaller than the factor 6 difference observed in experiment.

Rather than finding ourselves in the transition between the ion-limited and precursor-limited regimes as we expected for a dwell time of 4.8 ms, the precursor layer is nearly saturated and thus the growth must be ion-limited. In the ion-limited regime, we expect that an increase in ion dosage per unit length along the pillar (β/α) leads to a proportional increase in volume. This proportionality with volume manifests as a square root dependence with pillar width, which can be seen in figure 12 as the slope of the pillar radius is roughly half that of the reference line, affirming the ion-limited nature of this set of parameters.

It is understandable that n_{sat} closely mimics the behaviour of β, as they are both proportional to the number of depositions, and n_{sat} cannot differentiate itself without significant diffusion or deposition mechanisms at play.

It is also quite natural that γ and D have very little effect on the shape of the pillar in this regime: Since the precursor layer is so saturated, very little increase of precursors can occur due to adsorption or diffusion.

Pillar width increasing with larger λ_e is expected since larger λ_e means the SE flux contour surfaces are proportional to λ_e. However, the pillar width is not proportional to λ_e since wider pillars also need more SE flux to sustain the higher volumetric growth.

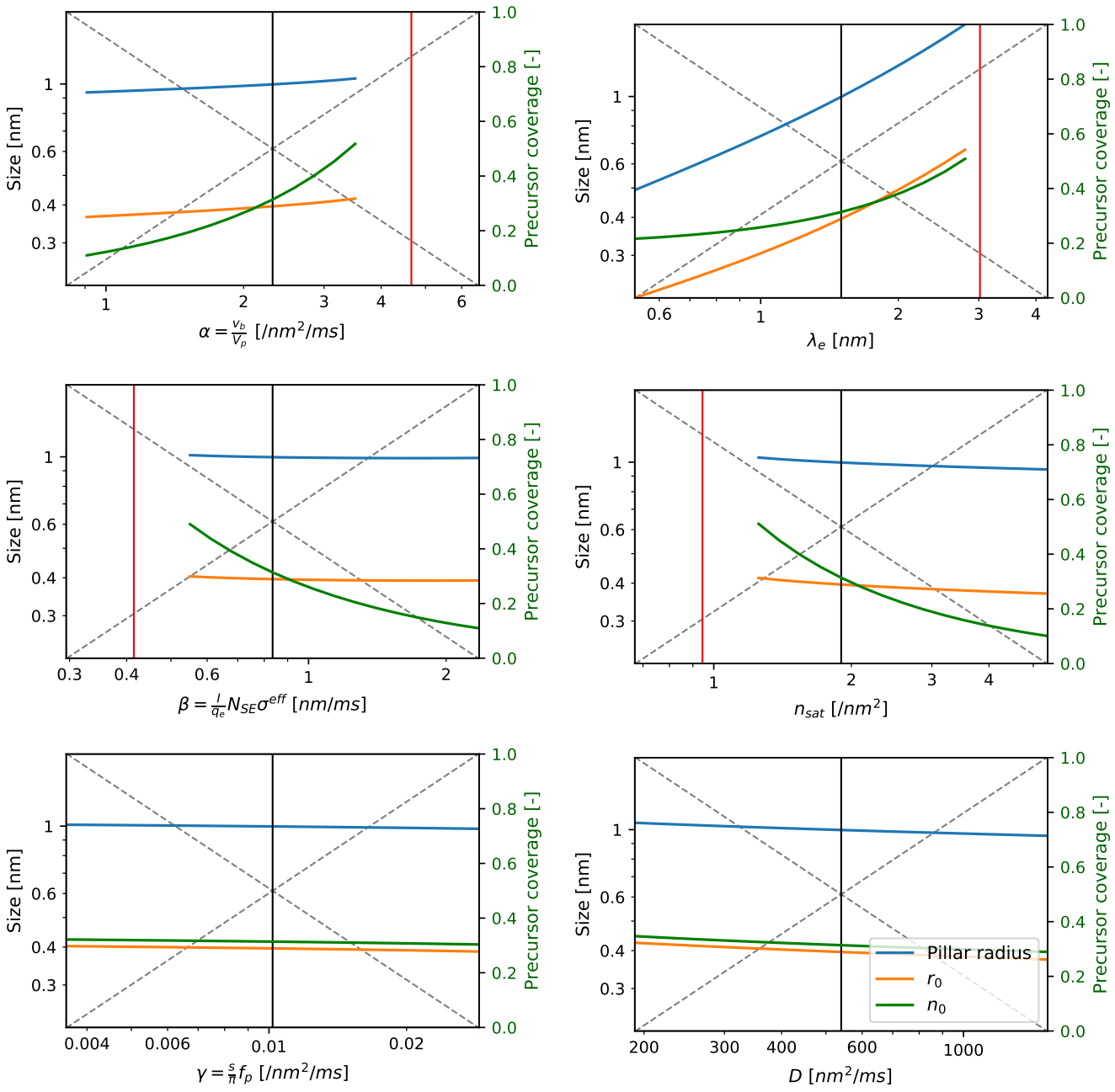

Figure 11: Sensitivity analysis on the 6 parameters for the small solution. The vertical black line indicates the default value (which is used for that parameter in the plots for other parameters). The grey dashed lines forming a cross are reference lines used for judging proportionality; if the size follows the same slope, it is proportional to either the parameter or its multiplicative inverse, respectively. The red line indicates the estimated nucleation boundary via equation 41.

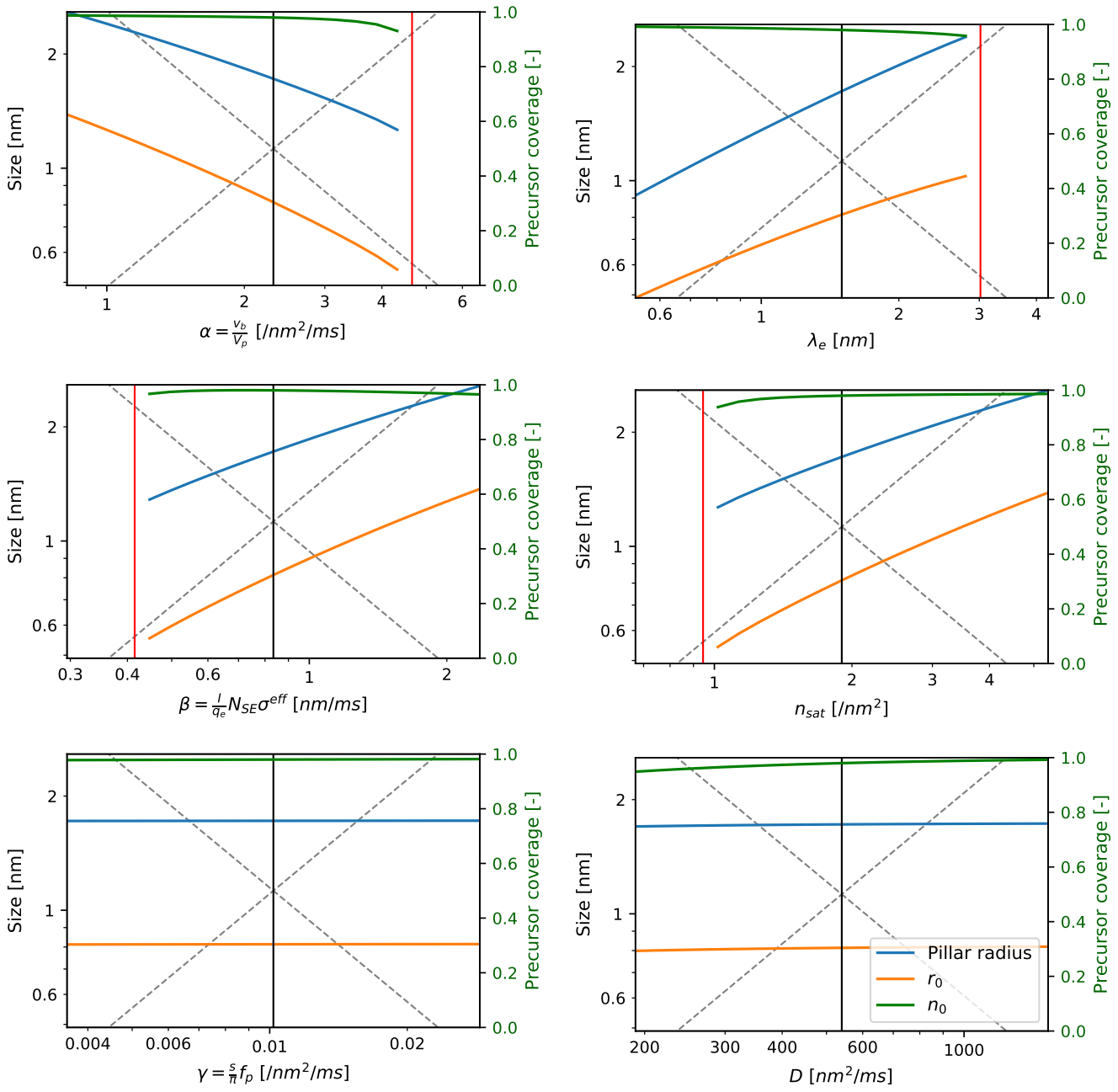

Figure 12: Sensitivity analysis on the 6 parameters for the large solution. The vertical black line indicates the default value (which is used for that parameter in the plots for other parameters). The grey dashed lines forming a cross are reference lines used for judging proportionality; if the size follows the same slope, it is proportional to either the parameter or its multiplicative inverse, respectively. The red line indicates the estimated nucleation boundary via equation 41.

β seems to be close to some kind of local optimum regarding the precursor coverage at the tip n_0, but it is still not clear that decreasing α (increasing dwell time) will eventually lead to a precursor limited regime.

It is notable that in all these sensitivity plots, the pillar radius seems to be consistently close to double that of the distance of the tip to the beam r_0. This may be a useful rule of thumb in considerations of discrete beam step sizes: For pillars of some diameter d, the step size should at most be $d/4$.

6 Conclusion

We found the nucleation boundary below which no growth occurs:

$$\frac{n_{sat}\beta}{\alpha\lambda_e} \gtrsim 0.227$$

(equation 41). The value corresponds to a dwell time of 2.4 ms when using the parameters of table 1, which is reasonably close to the experimentally observed [1] value of 4 ms, given the large uncertainties in the parameters involved.

The transition between ion-limited and precursor-limited growth was not observed at dwell time values near that of the experiment. It is likely that there is still a precursor-limited regime at much smaller α values. However, given that the pillar diameters observed in the model is roughly a factor 10 thinner than the experimentally observed pillars, there are clearly large inaccuracies at play, and only lowering the α value may not lead to more accurate results.

Roughly based on the sensitivity analysis results, inaccuracy of the physical constants used is likely insufficient to explain the amount of deviation we see here, as multiple coefficients would have to be changed by large amounts to approach the observed pillar widths. The most apparent culprit causing these inaccurately small pillars is the assumption that the ion beam has no width: The full-width-at-half-maximum of the ion distribution in the beam is approximately 1 nm [19], the tails would still have a significant contribution, as they would coincide with less depleted parts of the pillar tip. This means that realistically, significant SE production occurs over an area multiple nanometers in diameter, of similar or greater size than the pillars calculated here. This indicates that a more accurate ion beam profile would certainly result in wider pillars.

On the other hand is the omitted mechanism of stimulated desorption. [4] estimates "ten times as many precursors are lost by beam-induced desorption than by decomposition." Including this mechanism in the model would be equivalent to decreasing the growth volume per deposition V_p—and by thus increasing α—by a factor of 10. Unfortunately this can not explain the observed size discrepancy with experiment, as larger α would mean even smaller pillars.

A more accurate (3D with diffusion and desorption) model or simulation would be needed to confirm or deny whether the assumptions made are indeed excessive, and decide more conclusively whether the accuracy of the physical constants may be to blame. If a Monte-Carlo simulation is used, testing the effects of a diffuse beam should be relatively simple, as it simply means adding some stochasticity to the ion starting location.

We have also observed concrete indications that one of the assumptions that was made was stricter than intended, leading to not properly accounting for diffusion in the circumferential direction of the pillar. Rather than increasing the ODE complexity further by including even higher order derivatives, the problem is likely to be solved by modelling the full 2D surface instead, and solving a PDE. In other words, rather than making some simplifying assumption to determine n_{wwww}, periodic boundary conditions should be used to pin down the angular

diffusion; there should be no need for calculation of higher order derivatives. This problem is not so easily transferred to a PDE, however: The geodesic polar parametrisation is likely to run into problems, since the geodesics eventually overlap when the pillar is non-isotropic, making periodic boundary conditions difficult to enforce—among other issues. Using an irregular finite element mesh might be required, but a parametrisation is still needed since the shape of the surface is not known a priori. Furthermore, the ingress/egress location of the beam is not known a priori, so dynamic element generation is required.

Monte Carlo simulation is still a very powerful option to simulate this growth, but current models do not include precursor diffusion effects (and it may not be simple to include given the inherently non-smooth surfaces). The continuum model we have partly explored could—given expansion into a full 3D simulation and SE flux with a full range of energies—lead to more accurate results, since diffusion and other effects may be easier to include.

New differentiable programming techniques [33] mean that if we can develop a reliable differentiable simulation of IBID growth via the integration of differential equations, it may eventually be possible to combine this simulation with machine learning to invert the problem. Which would mean that a user could insert a desired 3D structure into some software, and it would calculate the beam movements required to produce the structure. This would clearly be more difficult with a stochastic simulation like Monte Carlo.

References

[1] G. Nanda, E. van Veldhoven, D. Maas, H. Sadeghian, and P. F. A. Alkemade, "Helium ion beam induced growth of hammerhead afm probes," *Journal of Vacuum Science & Technology B*, vol. 33, no. 6, p. 06F503, 2015.

[2] T. Betancourt and L. Brannon-Peppas, "Micro- and nanofabrication methods in nanotechnological medical and pharmaceutical devices," *International journal of nanomedicine*, vol. 1, pp. 483–95.

[3] J. Orloff, M. Utlaut, and L. Swanson, *Applications of Focused Ion Beams*, pp. 205–290. Boston, MA: Springer US, 2003.

[4] P. F. A. Alkemade and H. Miro, "Focused helium-ion-beam-induced deposition," *Applied Physics A, Materials Science and Processing*, vol. 117, no. 4, pp. 1727–47, 2014.

[5] S. Matsui, "Focused-ion-beam chemical-vapor-deposition (fib-cvd)," in *Encyclopedia of Nanotechnology* (B. Bhushan, ed.), pp. 1–14, 2014.

[6] I. Utke, P. Hoffmann, and J. Melngailis, "Gas-assisted focused electron beam and ion beam processing and fabrication," *Journal of Vacuum Science & Technology B: Microelectronics and Nanometer Structures Processing, Measurement, and Phenomena*, vol. 26, no. 4, pp. 1197–1276, 2008.

[7] D. A. Smith, D. C. Joy, and P. D. Rack, "Monte carlo simulation of focused helium ion beam induced deposition," *Nanotechnology*, vol. 21, p. 175302, apr 2010.

[8] R. Timilsina and P. D. Rack, "Monte carlo simulations of focused ion beam induced processing," in *Helium Ion Microscopy*, pp. 89–118, Springer, 2016.

[9] R. Timilsina, D. A. Smith, and P. D. Rack, "A comparison of neon versus helium ion beam induced deposition via monte carlo simulations," *Nanotechnology*, vol. 24, no. 11, p. 115302, 2013.

[10] P. F. Alkemade, P. Chen, E. van Veldhoven, and D. Maas, "Model for nanopillar growth by focused helium ion-beam-induced deposition," *Journal of Vacuum Science & Technology B, Nanotechnology and Microelectronics: Materials, Processing, Measurement, and Phenomena*, vol. 28, no. 6, pp. C6F22–C6F25, 2010.

[11] M. Deserno, "Notes on differential geometry with special emphasis on surfaces in r3," *Los Angeles, USA*, 2004.

[12] P. F. Alkemade, H. Miro, E. Van Veldhoven, D. J. Maas, D. A. Smith, and P. D. Rack, "Pulsed helium ion beam induced deposition: A means to high growth rates," *Journal of Vacuum Science & Technology B, Nanotechnology and Microelectronics: Materials, Processing, Measurement, and Phenomena*, vol. 29, no. 6, p. 06FG05, 2011.

[13] D. Smith, J. Fowlkes, and P. Rack, "A nanoscale three-dimensional monte carlo simulation of electron-beam-induced deposition with gas dynamics," *Nanotechnology*, vol. 18, no. 26, p. 265308, 2007.

[14] P. Chen, E. van Veldhoven, C. A. Sanford, H. W. Salemink, D. J. Maas, D. A. Smith, P. D. Rack, and P. F. Alkemade, "Nanopillar growth by focused helium ion-beam-induced deposition," *Nanotechnology*, vol. 21, no. 45, p. 455302, 2010.

[15] V. Friedli, C. Santschi, J. Michler, P. Hoffmann, and I. Utke, "Mass sensor for in situ monitoring of focused ion and electron beam induced processes," *Applied physics letters*, vol. 90, no. 5, p. 053106, 2007.

[16] E. Cawthron, "Secondary electron emission from solid surfaces bombarded by medium energy ions," *Australian Journal of Physics*, vol. 24, no. 4, pp. 859–870, 1971.

[17] W. Van Dorp, J. Wnuk, J. Gorham, D. Fairbrother, T. Madey, and C. Hagen, "Electron induced dissociation of trimethyl (methylcyclopentadienyl) platinum (iv): Total cross section as a function of incident electron energy," *Journal of Applied Physics*, vol. 106, no. 7, p. 074903, 2009.

[18] Y. V. Petrov, O. Vyvenko, and A. Bondarenko, "Scanning helium ion microscope: Distribution of secondary electrons and ion channeling," *Journal of Surface Investigation. X-ray, Synchrotron and Neutron Techniques*, vol. 4, no. 5, pp. 792–795, 2010.

[19] P. Chen, "Three-dimensional nanostructures fabricated by ion-beam-induced deposition," 2010.

[20] O. Y. Ridzel, V. Astašauskas, and W. S. Werner, "Low energy (1–100 ev) electron inelastic mean free path (imfp) values determined from analysis of secondary electron yields (sey) in the incident energy range of 0.1–10 kev," *Journal of Electron Spectroscopy and Related Phenomena*, vol. 241, p. 146824, 2020.

[21] D. Emfietzoglou, I. Kyriakou, R. Garcia-Molina, and I. Abril, "Inelastic mean free path of low-energy electrons in condensed media: beyond the standard models," *Surface and Interface Analysis*, vol. 49, no. 1, pp. 4–10, 2017.

[22] J. Hong and D. Mills, "Spin dependence of the inelastic electron mean free path in fe and ni: Explicit calculations and implications," *Physical Review B*, vol. 62, no. 9, p. 5589, 2000.

[23] H. T. Nguyen-Truong, "Low-energy electron inelastic mean free path in materials," *Applied Physics Letters*, vol. 108, no. 17, p. 172901, 2016.

[24] R. Zdyb, T. Menteş, A. Locatelli, M. Niño, and E. Bauer, "Inelastic mean free path from reflectivity of slow electrons," *Physical Review B*, vol. 87, no. 7, p. 075436, 2013.

[25] M. P. Seah and W. Dench, "Quantitative electron spectroscopy of surfaces: A standard data base for electron inelastic mean free paths in solids," *Surface and interface analysis*, vol. 1, no. 1, pp. 2–11, 1979.

[26] J. Bezanson, A. Edelman, S. Karpinski, and V. B. Shah, "Julia: A fresh approach to numerical computing," *SIAM review*, vol. 59, no. 1, pp. 65–98, 2017.

[27] C. Rackauckas and Q. Nie, "Differentialequations.jl a performant and feature-rich ecosystem for solving differential equations in julia," *The Journal of Open Research Software*, vol. 5, no. 1, 2017. Exported from https://app.dimensions.ai on 2019/05/05.

[28] C. Tsitouras, "Explicit runge–kutta methods for starting integration of lane–emden problem," *Applied Mathematics and Computation*, vol. 354, pp. 353–364, 2019.

[29] P. Bogacki and L. F. Shampine, "An efficient runge-kutta (4, 5) pair," *Computers & Mathematics with Applications*, vol. 32, no. 6, p. 1528, 1996.

[30] S. G. Johnson, "QuadGK.jl: Gauss–Kronrod integration in Julia." `https://github.com/JuliaMath/QuadGK.jl`.

[31] J. Revels, M. Lubin, and T. Papamarkou, "Forward-mode automatic differentiation in Julia," *arXiv:1607.07892 [cs.MS]*, 2016.

[32] S. Olver and A. Townsend, "A practical framework for infinite-dimensional linear algebra," in *Proceedings of the 1st Workshop for High Performance Technical Computing in Dynamic Languages – HPTCDL '14*, IEEE, 2014.

[33] M. Innes, A. Edelman, K. Fischer, C. Rackauckas, E. Saba, V. B. Shah, and W. Tebbutt, "A differentiable programming system to bridge machine learning and scientific computing," *arXiv preprint arXiv:1907.07587*, 2019.